Optical enhancement of dielectric permittivity in reduced lanthanum aluminate

Takayuki Nagai,[1,*] Akihide Kuwabara,[2] Yu Kumagai,[3] Ichiro Terasaki,[1] and Hiroki Taniguchi[1,†]
[1]Department of Physics, Nagoya University, Nagoya 464-8602, Japan
[2]Nanostructures Research Laboratory, Japan Fine Ceramics Center, Nagoya 456-8587, Japan
[3]Laboratory for Materials and Structures, Tokyo Institute of Technology, Yokohama 226-8503, Japan

(Received 13 December 2019; revised manuscript received 20 April 2020; accepted 22 April 2020; published 19 May 2020)

When light is absorbed in solids, electrical conductivity is usually enhanced through generation of photodoped conductive carriers, known as photoconduction. Here we show UV-light absorption restrains photoconduction, but markedly enhances dielectric permittivity in a ceramic sample of $LaAlO_3$ with defects introduced deliberately by reduction synthesis. Using systematic dielectric measurements under photoirradiation combined with computational studies for defect formation energies, we explain this unconventional photoinduced phenomenon in terms of photoexcited dipoles: The photoexcited electrons are trapped in in-gap states introduced by oxygen vacancies whereas photoexcited holes are localized in a valence-band maximum. Thus the created electron-hole pair acts as an electric dipole to enhance the dielectric permittivity. This unprecedented photoelectric effect does not only provide an alternative functionality for dielectric materials, but also paves the way for next-generation photoelectronic devices.

DOI: 10.1103/PhysRevB.101.184114

I. INTRODUCTION

Novel functionalities of materials have opened new frontiers in electronics as history illustrates. For instance, the discovery of ferroelectricity led to innovative device elements such as a ferroelectric random-access memory [1]. Also, photoinduced changes of physical properties have been used to connect optics and electronics. For example, an optical change in electric conductivity, known as “photoconduction,” has been applied in various photosensing devices. The photo-Seebeck effect, a change in the Seebeck coefficient caused by photodoped carriers, has recently been applied to achieve excellent thermoelectric efficiency via photoirradiation [2,3]. These photoinduced phenomena are caused by the contribution of photodoped conductive carriers. If mobility of the photodoped conductive carriers is sufficiently low, they would be localized, and contribute to the dielectric properties rather than the transport properties. Here, we demonstrate marked photoinduced enhancement of the dielectric permittivity in reduced $LaAlO_3$ (RLAO), which is caused by the photodoped localized carriers. Since dielectric materials are used ubiquitously as capacitors, frequency filters, and gate-insulating layers for metal-oxide-semiconductor transistors, the optical tuning of dielectric properties would provide a route to the development of innovative photoelectronic devices.

Photoinduced changes in the dielectric permittivity [photodielectric effect (PDE)] have been reported to date in quantum paraelectrics, [4–6] sulfide phosphors [7,8], and other materials [9–11]. In particular, a marked increment in the dielectric permittivity was reported in quantum paraelectric $SrTiO_3$ under illumination using ultraviolet light [4], and the dielectric permittivity was enhanced by photoirradiation up to 10^6 with the aid of an external dc-bias electric field [5]. Several mechanisms have been proposed to explain the PDE in $SrTiO_3$, including response of photoinduced polar nanodomains [4] or photocarriers trapped at in-gap states [12]. Follow-up studies, however, have revealed an extrinsic origin of PDE in $SrTiO_3$ due to photoconduction [13], which leads to severe increase in dielectric loss, causing fatal deterioration of material properties for practical applications.

A unique photoinduced change in the permittivity has recently been reported in some polycrystalline aluminates [14–16]. The dielectric permittivity of Zn:$LaAlO_3$ was found to increase with photoirradiation over a wide frequency range, up to at least 10^6 Hz. The observed small incremental change in dielectric loss tangent ($\tan\delta$) upon photoirradiation eliminated the extrinsic contribution of photoconduction, and suggests an intrinsic nature for the PDE in Zn:$LaAlO_3$ [14]. The mechanism responsible for the intrinsic PDE, however, remains an open question, and the photoinduced variation of the dielectric permittivity in Zn:$LaAlO_3$ is only approximately 7%.

In the present study, we demonstrate a markedly enhanced PDE in reduced polycrystalline RLAO, which is synthesized in a weak reducing atmosphere. The dielectric permittivity of this material is significantly enhanced over the frequency range from 10^2 to 10^6 Hz under photoirradiation with an incident photon energy of 3.4 eV. The simultaneous incremental dielectric loss is negligible, thereby indicating the intrinsic nature of the observed PDE. The origin of the PDE may stem from the dielectric response of photodoped localized carriers that are trapped in deep in-gap states introduced by the reduction synthesis. First-principles calculations show that

*Present address: Materials Research Center for Element Strategy, Tokyo Institute of Technology, Yokohama 226-8503, Japan.
†Corresponding author: hiroki_taniguchi@cc.nagoya-u.ac.jp

 ©2020 American Physical Society

these deep in-gap states originate from oxygen vacancies. The present findings thus provide guidelines for exploring novel dielectric materials with the PDE and support future developments of innovative phototunable devices.

II. EXPERIMENTAL AND COMPUTATIONAL METHODS

$LaAlO_3$ (LAO) and reduced $LaAlO_3$ (RLAO) were fabricated using a conventional solid-state reaction method. Stoichiometric mixtures of La_2O_3 (3N, Kojundo Chemical Laboratory Co. Ltd.) and Al_2O_3 (4N, Kojundo Chemical Laboratory Co. Ltd.) were ground in ethanol using an agate mortar and pestle, and they were then pelletized by dry pressing to diameters of 10 mm. The LAO and RLAO were synthesized at 1673 K for 12 h in air and 1673 K for 12 h in a nitrogen atmosphere, respectively. For the synthesis of RLAO, nitrogen gas was introduced into the furnace with a flow rate of 300 ml min^{-1}.

XRD measurements were performed at room temperature using a Rigaku RINT-2200 diffractometer. The dielectric properties were measured with an Agilent precision LCR meter E4980A from 10^2 to 10^6 Hz. For the dielectric measurements, the samples were polished to a thickness of 200 μm and gold electrodes were sputtered on both sides. The thickness of the upper electrode was 300 Å, which was semitransparent to the incident light (transmittance is around 50%). A light-emitting diode (LED) emitting photons with energy of 3.4 eV (Hamamatsu Photonics K. K. LC-L2) and a spectroscopic light source (Asahi Spectra Co. Ltd. MA-X303) were used as the light sources. To measure the sample temperature accurately during the PDE measurements, we used a homemade system equipped with an infrared thermometer (Keyence IT-02) that enabled monitoring of the local temperature of the photoirradiated area throughout the measurements [14,17]. The temperature of the sample surface was precisely controlled using a Peltier temperature controller (Funakoshi Co. Ltd. Model IC25) to maintain a similar sample temperature in both the dark and photoirradiated states. Note that the irradiated light covered the entire sample including the electroded area.

First-principles calculations were performed using the projector augmented wave (PAW) method [18,19], as implemented in the VASP code [20–23]. The configurations of the valence electrons in the PAW potentials were $5s^2\,5p^6\,6s^2\,5d^1$ for La, $3s^2\,3p^1$ for Al, and $2s^2\,2p^4$ for O, respectively. The HSEsol-type hybrid functional [21] was adopted in this study. For a primitive cell of LAO, the cutoff energy of the plane-wave basis sets and the mesh size for k-point sampling in the Brillouin zone were set to 500 eV and Γ-centered $4 \times 4 \times 4$, respectively. The lattice constants and internal atomic positions were fully optimized until all residual forces became <0.02 eV Å^{-1}. The optimized lattice constants for a conventional hexagonal cell were $a = 5.325$ Å and $c = 12.975$ Å. In comparison with data from the literature [24], our HSEsol calculation underestimated the lattice constants of LAO by about 1%.

To evaluate the formation energies of the point defects, supercell models were constructed from a hexagonal conventional unit cell of LAO; the size of the supercell was $2 \times 2 \times 1$ of the unit cells including 120 atoms. In the calculations for the supercells, the cutoff energy for the plane-wave basis sets was 400 eV, and one k point of $(\frac{1}{4}\ \frac{1}{4}\ \frac{1}{4})$ was sampled in the Brillouin zone.

The formation energies of the point defects were evaluated as [25]

$$E_{\text{f}}(\text{D}^q) = \{E_{\text{sup}}(D^q) + E_{\text{corr}}(D^q)\} - E_{\text{sup}}^{\text{perfect}} - \sum_i \Delta n_i \mu_i + q(\varepsilon_{\text{VBM}} + \Delta\varepsilon_{\text{F}}), \quad (1)$$

where $E_{\text{sup}}(D^q)$ and $E_{\text{sup}}^{\text{perfect}}$ are the total energies of a defect supercell that includes point defect D in charge state q and of a perfect supercell, respectively. $E_{\text{corr}}(D^q)$ is the image-charge correlation for charged defects. The energies of charge-defect supercells were corrected using the extended Freysoldt-Neugebauer–Van de Walle (FNV) scheme developed by Kumagai and Oba [25–27]. The quantities μ_i and Δn_i are the chemical potential and the difference in the numbers of atoms i between the defect and perfect supercells, respectively. For interstitial (vacancy) defects, Δn_i is positive (or negative). The quantity ε_{VBM} is the energy level of the VBM, and $\Delta\varepsilon_{\text{F}}$ corresponds to the Fermi energy as measured from ε_{VBM}. The dielectric tensors were calculated via the linear-response method [28] using the Perdew-Burke-Ernzerhof generalized-gradient approximation [29]. The calculated values for the ion-clamped dielectric tensors are $\varepsilon_{xx}^{\text{el}} = \varepsilon_{yy}^{\text{el}} = 4.74$, and $\varepsilon_{zz}^{\text{el}} = 4.66$. The ionic contributions were $\varepsilon_{xx}^{\text{ion}} = \varepsilon_{yy}^{\text{ion}} = 19.58$ and $\varepsilon_{zz}^{\text{ion}} = 24.35$.

The chemical potentials μ_i were determined under phase-equilibrium conditions. First, RLAO was assumed to be equilibrated in an oxygen atmosphere, and nonstoichiometric conditions of the cations, where La_2O_3 or Al_2O_3 coexists with $LaAlO_3$, were taken into account. For La_2O_3-rich conditions, the following relations hold for the total energies of the coexisting phases and chemical potentials:

$$\begin{aligned} \mu_{\text{La}_2\text{O}_3} &= 2\mu_{\text{La}} + 3\mu_{\text{O}}, \\ \mu_{\text{LaAlO}_3} &= \mu_{\text{La}} + \mu_{\text{Al}} + 3\mu_{\text{O}}, \\ \mu_{\text{O}_2(\text{g})} &= 2\mu_{\text{O}}. \end{aligned} \quad (2)$$

We can uniquely determine the values of the chemical potentials from the total energies of La_2O_3, $LaAlO_3$, and $O_2(g)$. When the Al_2O_3-rich condition was considered, the total energy term for Al_2O_3 was substituted for that of La_2O_3. Assuming that the oxygen behaves as an ideal gas, the value of μ_{O_2} at a specified temperature and partial pressure were given by [30]

$$\mu_{\text{O}_2}(T,\ p) = E_{\text{O}_2}^{\text{HSEsol}} + \Delta H_{\text{O}_2}(T,\ p^0) - TS_{\text{O}_2}(T,\ p^0) + k_{\text{B}}T \ln \frac{p}{p^0}, \quad (3)$$

where $E_{\text{O}_2}^{\text{HSEsol}}$ is the total energy of an O_2 molecule at 0 K calculated using our HSEsol calculations, and the thermodynamics parameters such as the enthalpy $\Delta H_{\text{O}_2}(T,\ p^0)$ relative to that at 0 K and the entropy $S_{\text{O}_2}(T,\ p^0)$ at temperature T and pressure p^0 are taken from Ref. [31].

III. RESULTS AND DISCUSSION

The crystallographic phases of the sintered samples were identified via x-ray diffraction (XRD) measurements. Figure S1 (see Supplemental Material [32]) compares the XRD patterns of the polycrystalline RLAO and LAO at room temperature and the simulated pattern generated via RIETAN-FP [33], using the lattice parameters of $LaAlO_3$ reported previously [24]. Both patterns are in excellent agreement with the calculated pattern, indicating rhombohedral symmetry (space group $R\bar{3}c$) for all samples. A slight impurity phase of La_2O_3 was observed in RLAO, and the diffraction peaks for this phase are marked with asterisks in Fig. S1 [32]. This impurity may be caused by compensation for oxygen vacancies formed under the reducing conditions. The simultaneous generation of an Al_2O_3 impurity is also likely, although it was not detected, probably because of its weak intensity.

Figure 1 shows frequency dispersion of a real part (ε', top panel) and an imaginary part (ε'', bottom panel) of complex permittivity, which were observed in (a) RLAO and (b) LAO, respectively. Circles and squares in the panels represent data points observed in dark and irradiated states, respectively. In the irradiated states, the samples were illuminated using the LED with an irradiation intensity of $175\,\mathrm{mW\,cm^{-2}}$ on the sample. Note that the energy of the photons, 3.4 eV ($\lambda = 365\,\mathrm{nm}$), was chosen to be smaller than the band-gap energy of LAO ($E_g = 5.6\,\mathrm{eV}$) [34]. The sample temperature was kept at 340 K using a Peltier temperature controller in both the dark and irradiated states. As shown in Figs. 1(a) and 1(b), ε' and ε'' in the dark state are similar between RLAO and LAO ($\varepsilon' \sim 20$) over the frequency range observed in the present study. Note here that, in $\tan\delta (\equiv \varepsilon''/\varepsilon')$ which indicates energy loss of charge/discharge, as presented in Fig. S2 (see Supplemental Material [32]), a broad peak is observed around 10^5 Hz in RLAO. This peak possibly stems from the Maxwell-Wagner effect owing to the spatial inhomogeneity of the conductivity between grains and grain boundaries [35] or from the depletion layers at the sample-electrode interfaces owing to Schottky contact [36]. Since the peak is very weak, the possible inhomogeneities would have negligible influence on the insulating property of the material. Under the photoirradiation, on the other hand, a significant enhancement of the dielectric permittivity ε' of RLAO is found over the entire frequency range up to 10^6 Hz as clearly shown in the top panel of Fig. 1(a). In particular, the enhancement at 10^6 Hz reaches approximately 100%, which is more than ten times greater than those reported for Zn:LAO [14]. In the photoirradiated state, as seen in the figure, ε' shows a similar frequency dispersion as that observed in the dark state. This result suggests that the photoinduced component has little frequency dispersion at least until the upper frequency limit of the present study of 10^6 Hz. The photoinduced component would decay in the higher-frequency range to show the corresponding dielectric relaxation. As presented in the bottom panel of Fig. 1(a), the photoinduced increment of the imaginary part is significantly weak compared to that of the real part. A relative change of the imaginary part can be discerned more clearly in the inset of Fig. 1(a) with a magnified scale. As shown in the inset, the imaginary part increases under the photoirradiation by 1–2 in the high-frequency region. Though growth rate of the imaginary part is somewhat larger than that of the real part, the quantitative increase is an order of magnitude smaller than the real part's; thereby enhancement of $\tan\delta$ is modest as shown in Fig. S2 (see Supplemental Material [32]). Furthermore, as shown in the inset of Fig. 1(a), only slight enhancement due to the Drude component, which generally grows divergently as the frequency approaches zero, is found in the low-frequency region below 10^3 Hz under the photoirradiation. This result suggests that there is a negligible contribution of photoconduction that causes undesired leakage current. Note that the broad peak of $\tan\delta$ observed in the dark state shifts to lower frequencies under photoirradiation as shown in Fig. S2 [32].

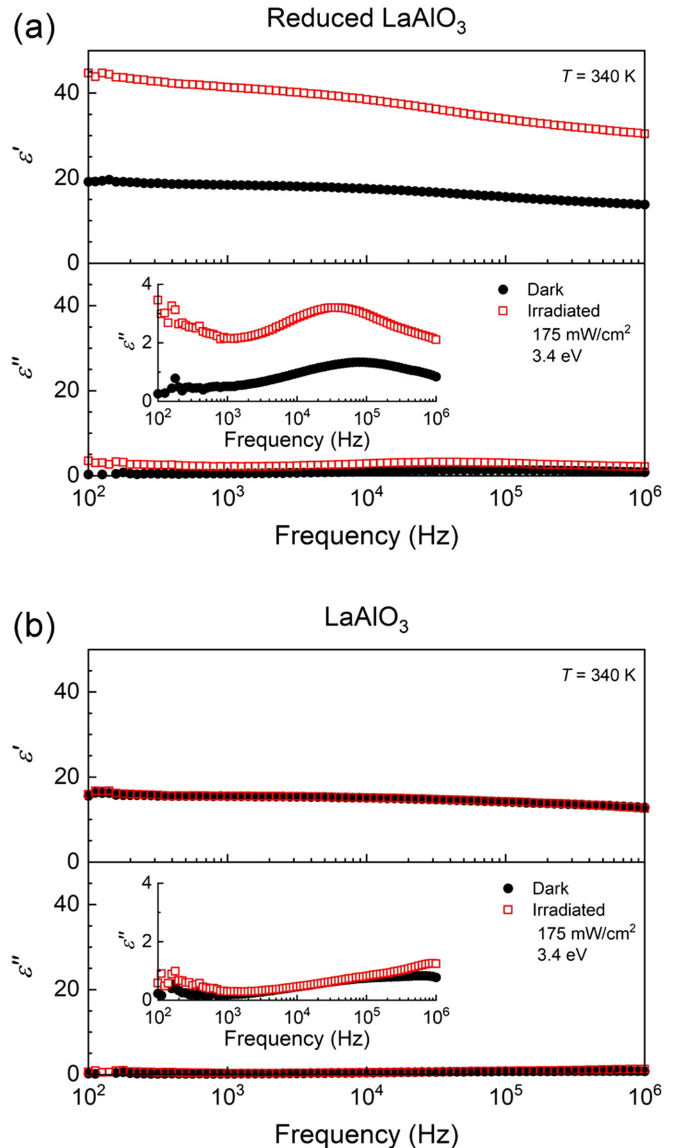

FIG. 1. The frequency dispersion of the dielectric properties observed in (a) reduced $LaAlO_3$, and (b) $LaAlO_3$, based on measurements taken shortly after illumination is turned on. Top and bottom panels show a real part and an imaginary part of complex dielectric permittivity, ε' and ε'', respectively. Circles and squares in the figure denote data observed in the dark state and the photoirradiated state, respectively. The insets in panels (a,b) show the imaginary part of complex dielectric permittivity in a magnified scale.

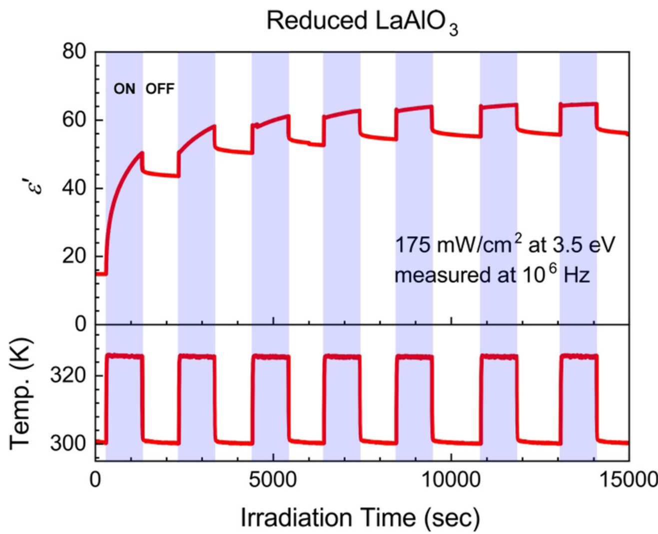

FIG. 2. (Top panel) A transient change in the real part of complex permittivity ε' for reduced $LaAlO_3$ observed under the photoirradiation with blinking LED. (Bottom panel) A transient change in the sample temperature measured using an infrared thermometer during the photoirradiation. The shaded regions in the panels denote the photoirradiated states.

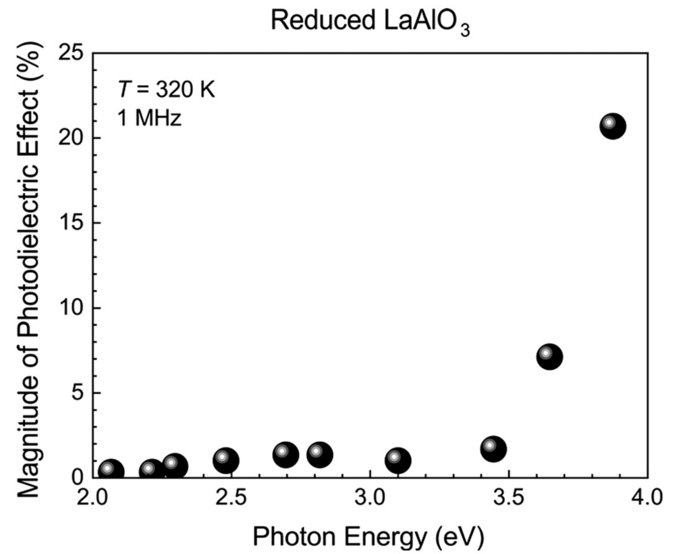

FIG. 3. The magnitude of PDE at 320 K measured under the photoirradiation of various photon energies.

Should the broad peak be caused by the Maxwell-Wagner effect, the peak frequency of tanδ, f_{peak}, is given by $f_{\mathrm{peak}} \propto (R_{\mathrm{b}} + R_{\mathrm{e}})/R_{\mathrm{b}}R_{\mathrm{e}}(C_{\mathrm{b}} + C_{\mathrm{e}})$ [35,37]. Here, R_{b} and C_{b}, respectively, denote resistance and capacitance in the regions where photoexcited carriers exist. R_{e} and C_{e}, respectively, denote resistance and capacitance in the barrier layers caused by factors such as grain boundaries and sample-electrode interfaces. The number of conductive carriers generally increases under photoirradiation, and the increment of carriers decreases the resistance R_{b}. This causes f_{peak} to shift to higher frequencies according to the formula above. This behavior, however, is incompatible with the present results. The shifting of f_{peak} to lower frequencies indicates that photoirradiation enhances the capacitance C_{b}, and this result strongly indicates an intrinsic origin for the photoinduced enhancement of the permittivity discovered in RLAO. In marked contrast, the dielectric properties of LAO remain unchanged under photoirradiation, as shown in Fig. 1(b).

The switching property of the PDE in RLAO was investigated using the blinking LED with the irradiation intensity of 175 mW cm^{-2} on the sample. The top panel in Fig. 2 shows the transient variations of ε' measured at 10^6 Hz. A simultaneous change in local temperature of the irradiated area is presented in the bottom panel for reference. As shown in the bottom panel, the sample temperature in the irradiated area increases immediately after switching on the LED. Although the temperature remains nearly constant during the photoirradiation, the value of ε' gradually increases with time, confirming that the enhancement of dielectric permittivity in RLAO is never caused by local heating due to the photoirradiation. Once the LED is turned off, ε' rapidly decreases by around 30% and then gradually decays with time. This demonstrates that the transient and persistent components provide two different contributions to the PDE in RLAO. Multiple contributions from photoexcited carriers with different relaxation processes were also suggested in the previous study of Zn:LAO [14]. Note that by 15 000 s after the first irradiation, the persistent change in ε' asymptotically reaches approximately 340% of its initial value.

Figure 3 shows the magnitude of PDE at room temperature, which is defined by $(\varepsilon'_{\mathrm{Photo}} - \varepsilon'_{\mathrm{Dark}})/\varepsilon'_{\mathrm{Dark}}$, as a function of the irradiated photon energy, where $\varepsilon'_{\mathrm{Photo}}$ and $\varepsilon'_{\mathrm{Dark}}$ are the real part of dielectric permittivity at 10^6 Hz measured in the photoirradiated and in the dark states, respectively. Intensity of the irradiated light was fixed at 0.04 mW cm^{-2} on the sample for each photon energy. As shown in the figure, the magnitude of PDE steeply grows as the photon energy increases from 3.5 eV, whereas it is negligibly weak in the range below 3.5 eV. This result suggests the existence of deep in-gap states more than 3.5 eV above the valence-band maximum (VBM). The observed threshold energy of irradiated photons to induce PDE is in good agreement with those obtained for Zn:LAO [14].

To clarify the origins of the in-gap states, optical transition energies for several types of defects expected in LAO were investigated with the first-principles calculations. The band-gap energy obtained in the present calculations is 5.50 eV, as shown in Fig. 4, which is in excellent agreement with the experimental value of 5.6 eV [34]. Two types of optical transitions were considered in the present study: excitation of electrons from occupied defect states to the conduction-band minimum, and excitation of electrons from the valence-band maximum to unoccupied defect states. Optical transition energies were calculated from the defect formation energies of the initial and final charge states. Based on the Franck-Condon principles, the atomic positions of final charge states were set to be the same as those of initial charge states [38]. Figures 4(a)–4(c) show optical transition energy diagrams for several possible defect states in LAO. Symbols of V_A and A_{i} (A = La, Al, or O) denote vacancy and interstitial defect states for A, respectively. La_{Al} (Al_{La}), on the other hand,

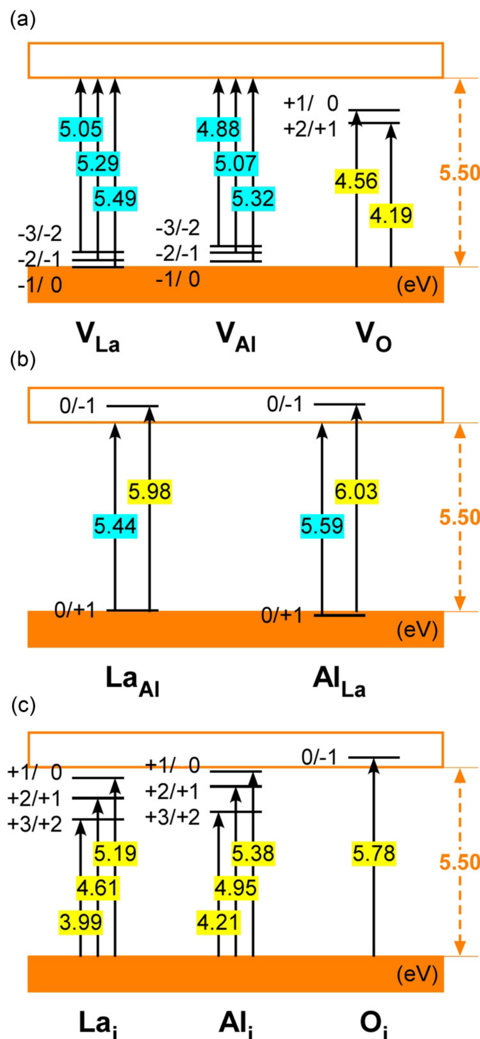

FIG. 4. Optical transition energies calculated for various defect states expected in $LaAlO_3$ including (a) vacancy, (b) cation antisite, and (c) interstitial-type defects.

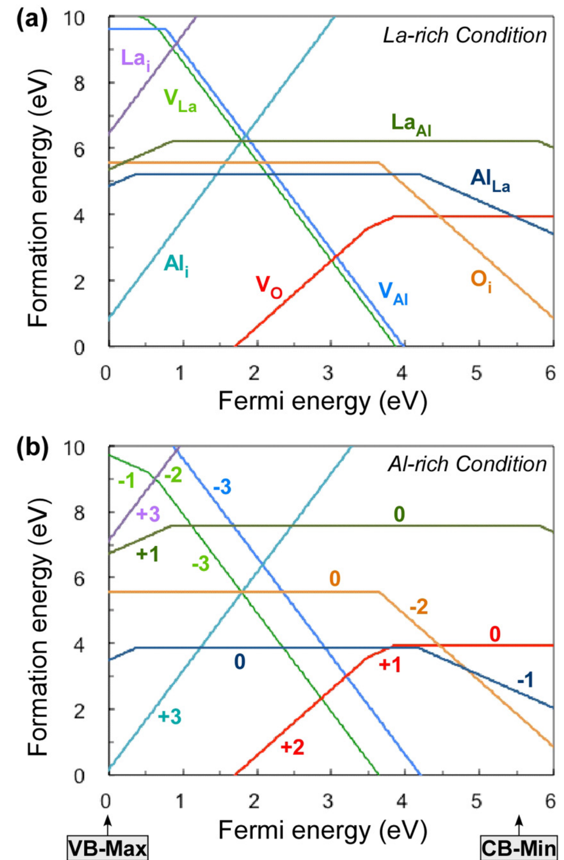

FIG. 5. Formation energies of various defects in $LaAlO_3$ plotted as a function of Fermi energy, which were calculated in (a) La-rich and (b) Al-rich conditions. Energy levels for a valence-band maximum (VB-Max) of 0.0 eV and a conduction-band minimum (CB-Min) of 5.5 eV are indicated by arrows in panel (b).

indicates a cation antisite defect, where a La site (Al site) is occupied by Al (La). As shown in Fig. 4, the energy levels of the cation vacancies (V_{La} and V_{Al}) are much shallower than the levels caused by the oxygen vacancies (V_O). These trends are in good agreement with previous results for cubic LAO (space group $Pm\bar{3}m$) [39]. The cation antisite defects of La_{Al} and Al_{La} never create deep in-gap states as presented in Fig. 4(b). As shown in Fig. 4(c), on the other hand, three defect states due to La_i locate at 3.99–5.19 eV above the VBM, whereas those for Al_i are around 4.21–5.38 eV above the VBM. Since the optical transition energies due to V_O (+2/+1), La_i (+3/+2), and Al_i (+3/+2) are relatively close to the threshold energy of 3.5 eV to induce PDE compared to the others', these defect states are potential candidates that play an important role in the observed PDE.

Figures 5(a) and 5(b) present the formation energies of the various defects as a function of the Fermi energy; they are calculated for La_2O_3-rich and Al_2O_3-rich conditions, respectively. Calculations were performed with a partial pressure of oxygen, p_{O_2}, of 10^{-5} atm and a temperature of 1700 K that is nearly equal to the present synthesis temperature of 1673 K for RLAO. The slope of the line reflects a charge state of defect, where the positive or the negative sign of each slope represents donor or acceptor type for the defects, respectively. Inflection points on the lines denote thermal transition energies between the different charge states [38]. Assuming charge neutrality, majority defects are obtained from intersections of the lines of the positively and negatively charged defects with the lowest formation energies. It can be found in Fig. 5(a) that the most stable defect combination that satisfies charge neutrality under the La-rich condition is a Schottky-type defect of $3V_O^{\cdot\cdot} + 2V_{La}^{'''}$, the corresponding intersection of which is located at approximately 3 eV above the VBM. This result is consistent with the results of XRD shown in Fig. S1 (see Supplemental Material [32]), in which the impurity peaks of La_2O_3 are detected even though the RLAO was synthesized with a stoichiometric powder mixture. The La_2O_3 impurity implies that La vacancies were generated to compensate charge unbalance due to oxygen vacancies introduced by the reduction synthesis. Since the Schottky defects $3V_O^{\cdot\cdot} + 2V_{La}^{'''}$ occur with almost the same formation energy as that for $3V_O^{\cdot\cdot} + 2V_{Al}^{'''}$, generation of $3V_O^{\cdot\cdot} + V_{La}^{'''} + V_{Al}^{'''}$ is also likely. Also in the Al-rich condition, as shown in Fig. 5(b), the Schottky defects $3V_O^{\cdot\cdot} + 2V_{La}^{'''}$ are more

preferable. The formation energies of cation interstitials $La_i^{\cdot}$ and $Al_i^{\cdot}$, which are the other candidates for the in-gap states effective to the observed PDE, on the other hand, are much higher than that for $V_O^{\cdot\cdot}$ as shown in Fig. 5. More specifically, the formation energies of the cation interstitials are higher than 8 eV at the Fermi energy of around 3 eV at which the Schottky defects $3V_O^{\cdot\cdot} + 2V_{La}'''$ form, whereas that for $V_O^{\cdot\cdot}$ is smaller than 3 eV. Therefore, the in-gap states due to cation interstitials, $La_i^{\cdot\cdot\cdot}$ and $Al_i^{\cdot\cdot\cdot}$, can be too scarce to contribute to the PDE observed in RLAO. Though many defect states are expected to be introduced in RLAO, the complementary results of the transition energy and the defect formation energy suggest that the oxygen vacancy plays a significant role in the PDE observed in RLAO. Note that, on increasing photon energy of the irradiated light, it is possible for the other optical transitions to take part in the PDE. In such a case also, the oxygen vacancy is a primary agent, judging from the energy diagram shown in Fig. 4. Compared to the observed threshold energy of irradiated photons to induce PDE, the theoretically obtained transition energy of V_O (+2/+1) is overestimated. This would be due to finite temperature effects such as thermal expansion and lattice vibration, which are not taken into account in our first-principles calculations.

According to the results of the present experiments and calculations, a plausible origin for the PDE is the dielectric response of a photoinduced electric dipole that stems from photoexcited electrons trapped at the defect states of oxygen vacancies, as also proposed in previous studies [14,40]. Conventional wisdom holds that photoinduced electrons function as conductive carriers under the application of electric fields, a phenomenon known as photoconductivity [41]. For RLAO, however, the photoinduced electrons are expected to be strongly localized in the in-gap states. Furthermore, the simultaneously created holes would also be localized, since the VBM in LAO mainly comprises flat bands owing to oxygen $2p$ orbitals. The weakly dispersive characters of the in-gap states and the VBM are shown in the supporting information (Figs. S2–S4 in the Supplemental Material [32]). Such strongly localized carriers would form the electron-hole pairs, which behave as electric polarization under the application of an electric field rather than conductive carriers. The small variation of tanδ under the photoirradiation is also consistent with the nonconductive feature of the photoexcited carriers, because tanδ would increase markedly in the low-frequency region if the photoexcited carriers are conductive. The individual origins for the transient and persistent components of the PDE are still unclear; however, they can be understood as counterparts of the transient and the persistent photoconductions if the proposed mechanism for the PDE is correct. In this sense, the PDE and photoconductivity are two sides of the same coin. They are distinguished by a difference in mobility of the photoexcited carriers owing to the character of the trapping defect states. The PDE is thus regarded as a novel internal photoelectric effect due to the localized photoexcited carriers. Further development of the PDE would thus be a matter of defect engineering.

IV. CONCLUSION

In summary, we have demonstrated the large photoinduced enhancement of the dielectric permittivity in reduced $LaAlO_3$ under photoirradiation. The dielectric permittivity is enhanced up to approximately 340% at 10^6 Hz with less incremental dielectric loss (tanδ). The excitation-energy dependence of the PDE in reduced $LaAlO_3$ suggests the existence of deep in-gap states at around 3.5 eV above the VBM. First-principles calculations have shown that the deep in-gap states stem from oxygen vacancies introduced by reduction synthesis. We consider that the large PDE in reduced $LaAlO_3$ is caused by the dielectric response of photoinduced dipoles, which are composed of strongly localized photoexcited carriers. The present findings provide an alternative functionality for dielectric materials and point towards the development of innovative opto-dielectric devices.

ACKNOWLEDGMENTS

This work was partially supported by a Grant-in-Aid for Challenging Exploratory Research (Grant No. 15K14120), MEXT Element Strategy Initiative Project. One of the authors (T.N.) was supported by the Program for Leading Graduate Schools “Integrative Graduate Education and Research in Green Natural Sciences,” MEXT, Japan, and a Grant-in-Aid for JSPS Research Fellow (Grant No. 18J11905), MEXT, Japan.

[1] G. H. Haertling, J. Am. Ceram. Soc. **82**, 797 (1999).
[2] I. Terasaki, R. Okazaki, and H. Ohta, Scr. Mater. **111**, 23 (2016).
[3] R. Okazaki, A. Horikawa, Y. Yasui, and I. Terasaki, J. Phys. Soc. Jpn. **81**, 114722 (2012).
[4] T. Hasegawa, S. Mouri, Y. Yamada, and K. Tanaka, J. Phys. Soc. Jpn. **72**, 41 (2003).
[5] M. Takesada, T. Yagi, M. Itoh, and S. Koshihara, J. Phys. Soc. Jpn. **72**, 37 (2003).
[6] I. Katayama, Y. Ichikawa, and K. Tanaka, Phys. Rev. B **67**, 100102(R) (2003).
[7] S. Kronenberg and C. A. Accard, Phys. Rev. **101**, 989 (1956).
[8] P. Krispin and W. Ludwig, Phys. Status Solidi **5**, 573 (1964).
[9] C. Masingboon, T. Eknapakul, S. Suwanwong, P. Buaphet, H. Nakajima, S.-K. Mo, P. Thongbai, P. D. C. King, S. Maensiri, and W. Meevasana, Appl. Phys. Lett. **102**, 202903 (2013).
[10] H. Taniguchi, H. Moriwake, A. Kuwabara, T. Okamura, T. Yamamoto, R. Okazaki, M. Itoh, and I. Terasaki, J. Appl. Phys. **115**, 164103 (2014).
[11] J. Juarez-Perez, R. S. Sanchez, L. Badia, G. Garcia-Belmonte, Y. S. Kang, I. Mora-Sero, and J. Bisquert, J. Phys. Chem. Lett. **5**, 2390 (2014).
[12] T. Mizokawa, N. Takaiwa, Y. Fujiwara, T. Iida, K. Takubo, J.-Y. Son, T. Ishikawa, M. Itoh, and M. Takesada, J. Phys. Soc. Jpn. **79**, 044703 (2010).
[13] Y. Yamada and K. Tanaka, J. Phys. Soc. Jpn. **77**, 054704 (2008).

[14] T. Nagai, H. Takahashi, R. Okazaki, K. Tanabe, I. Terasaki, and H. Taniguchi, Appl. Phys. Lett. **110**, 172901 (2017).
[15] T. Nagai, Y. Yamada, K. Tanabe, I. Terasaki, and H. Taniguchi, Appl. Phys. Lett. **111**, 232902 (2017).
[16] T. Nagai, K. Tanabe, I. Terasaki, and H. Taniguchi, Appl. Phys. Lett. **113**, 212902 (2018).
[17] R. Okazaki, Y. Nishina, Y. Yasui, F. Nakamura, T. Suzuki, and I. Terasaki, J. Phys. Soc. Jpn. **82**, 103702 (2013).
[18] P. E. Blöchl, Phys. Rev. B **50**, 17953 (1994).
[19] G. Kresse and D. Joubert, Phys. Rev. B **59**, 1758 (1999).
[20] G. Kresse and J. Hafner, Phys. Rev. B **47**, 558 (1993).
[21] G. Kresse and J. Furthmüller, Phys. Rev. B **54**, 11169 (1996).
[22] G. Kresse and J. Furthmüller, Comput. Mater. Sci. **6**, 15 (1996).
[23] L. Schimka, J. Harl, and G. Kresse, J. Chem. Phys. **134**, 024116 (2011).
[24] S. Geller and V. B. Bala, Acta. Crystallogr. **9**, 1019 (1956).
[25] Y. Kumagai and F. Oba, Phys. Rev. B **89**, 195205 (2014).
[26] C. Freysoldt, J. Neugebauer, and C. G. Van de Walle, Phys. Rev. Lett. **102**, 016402 (2009).
[27] Y. Kumagai, L. A. Burton, A. Walsh, and F. Oba, Phys. Rev. Appl. **6**, 014009 (2016).
[28] M. Gajdoš, K. Hummer, G. Kresse, J. Furthmüller, and F. Bechstedt, Phys. Rev. B **73**, 045112 (2006).
[29] J. P. Perdew, K. Burke, and M. Ernzerhof, Phys. Rev. Lett. **77**, 3865 (1996).
[30] K. Reuter and M. Scheffler, Phys. Rev. B **65**, 035406 (2001).
[31] M. W. Chase, Jr., *NIST-JANAF Thermochemical Tables*, 4th ed. (AIP, Melville, NY, 1998).
[32] See Supplemental Material at http://link.aps.org/supplemental/10.1103/PhysRevB.101.184114 for more details on experiments and calculations.
[33] F. Izumi and K. Momma, Solid State Phenom. **130**, 15 (2007).
[34] S. G. Lim, S. Kriventsov, T. N. Jackson, J. H. Haeni, D. G. Schlom, A. M. Balbashov, R. Uecker, P. Reiche, J. L. Freeouf, and G. Lucovsky, J. Appl. Phys. **91**, 4500 (2002).
[35] J. Liu, C. G. Duan, W. G. Yin, W. N. Mei, R. W. Smith, and J. R. Hardy, Phys. Rev. B **70**, 144106 (2004).
[36] P. Lunkenheimer, R. Fichtl, S. G. Ebbinghaus, and A. Loidl, Phys. Rev. B **70**, 172102 (2004).
[37] A. R. von Hippel, *Dielectrics and Waves* (The MIT Press, Cambridge, MA, 1954).
[38] S. Lany and A. Zunger, Phys. Rev. B **72**, 035215 (2005).
[39] M. Choi, A. Janotti, and C. G. Van de Walle, Phys. Rev. B **88**, 214117 (2013).
[40] W. H. Hartwig and J. J. Hinds, J. Appl. Phys. **40**, 2020 (1969).
[41] R. H. Bube and H. E. Macdonald, Phys. Rev. **121**, 473 (1961).